Dynamic topography and the nature of deep thick plumes

William D. Frazer and Jun Korenaga

Department of Earth and Planetary Sciences, Yale University

PO Box 208109, New Haven, CT 06520, USA

Abstract:

Deep mantle plumes imaged by seismic tomography have much larger radii (~400 km) than predicted by conventional geodynamic models (~100 km). Plume buoyancy fluxes estimated from surface topography concur with narrow plumes with low viscosities expected from their high temperatures. If plumes are thick as imaged by tomography, buoyancy flux estimates may require very viscous or thermochemical plumes. Here we assess the dynamical plausibility of an alternative model, a ponding plume, which has been suggested to explain thick plumes as well as buoyancy fluxes estimated from surface topography. In the ponding plume model, a thick conduit in the lower mantle narrows significantly after passing through the mantle transition zone, below which excess material from the thick lower-mantle plume, which cannot be accommodated by the narrow upper-mantle plume, spreads laterally. Such excess material in the mid-mantle, however, should still manifest itself in surface topography, the amplitude of which can be quantified via topography kernels. We find that the ponding of a purely thermal plume would lead to unrealistic excess topography, with the scale of ponding material large enough to be detected by seismic tomography. If mantle plumes are as thick as indicated by seismic topography, it appears to be necessary to deviate from either conventional temperature-dependent viscosity or the assumption of purely thermal origins.

Keywords: mantle plumes, hotspot swells, core heat flux

1. Introduction

Convective instabilities at the core-mantle boundary region can result in the formation of mantle plumes (Morgan, 1971). It is widely believed that mantle plumes are responsible for the formation of hotspot islands such as the Hawaiian Islands, the Azores, and the Marquesas Islands, and also for the significant topographic swells around them (e.g., Ballmer et al., 2015). The upwelling of mantle plumes is an important part of core heat flux as well (e.g., Davies, 1988; Labrosse, 2002; Zhong, 2006). Presently, however, there are significant discrepancies between the geodynamic models of mantle plumes and their actual images in seismic tomography. Geodynamic predictions typically suggest that well-developed plumes should have conduits of no more than 100 km in radius if they are of thermal origin (e.g., Richards et al., 1989). On the other hand, seismic tomography has imaged much thicker plume conduits in the lower mantle (Montelli et al., 2006; French and Romanowicz, 2015). Resolving the discrepancies between these models is important for a better understanding of plume dynamics and the origin of hotspot islands.

The amount of material transported by a plume can be quantified by buoyancy flux, which depends on the cross section of upwelling, the thermal buoyancy of the material, and its viscosity (Olson et al., 1993). Since buoyancy flux is proportional to the fourth power of the conduit radius, a small change in the size of the plume should result in substantial differences in surface topography (Korenaga, 2005). The buoyancy flux of plumes has long been estimated from swell topography (Davies, 1988; Sleep, 1990; King and Adam, 2014; Hoggard et al., 2020). Such topography-based estimates of buoyancy flux are consistent with the notion of a low-viscosity narrow conduit as predicted by geodynamic modeling. If plume conduits are as thick as suggested by seismic tomography, and if plumes have low viscosity, a much larger topographic response would be expected than is observed (Korenaga, 2005). At least three explanations may reconcile thick plume conduits at depth with the observed topographic swells. One end-member is a thick thermal plume with a very high viscosity brought by grain-size-sensitive creep (Figure 1a). A "firm" plume of this nature allows for a very thick plume conduit with buoyancy flux consistent with swell topography (Korenaga, 2005). Recently, it has been suggested that viscoplastic rheology in the lower mantle may generate think lower-mantle plumes (Davaille et al., 2018); this rheological effect on plume dynamics is similar to that of grain-size-sensitive creep, so it can be classified into this end-member. Alternatively, the presence of high-density eclogite in a thermochemical plume can sufficiently reduce buoyancy flux and may reconcile this discrepancy as well (Farnetani and Samuel, 2005; Lin and van Keken, 2006; Dannberg and Sobolev, 2015). Finally, a plume could be thick and have low viscosity, but most of the plume materials might be deflected in the mid-mantle, resulting in a narrow conduit in the upper mantle (Figure 1b; Nolet et al., 2006). Such deflection could potentially occur beneath the mantle transition zone (MTZ) where viscosity is thought to exhibit a large jump (e.g., Hager et al., 1985; Mitrovica and Forte, 2004; Liu and Zhong, 2016). Geodynamical modeling suggests that plumes narrow during upwelling through large viscosity contrasts (Richards et al., 1988; Farnetani and Richard, 1994; Leng and Gurnis, 2012). Additionally, there is seismic evidence suggesting that some plumes seem to have extra material ponding at the base of the MTZ in global tomography (Nolet et al., 2006) and regional tomography (Hansen et al., 2014). Under this ponding plume model, the buoyancy flux of the plume would be significantly reduced in the upper mantle. Conversely, the ponding plume model implies a much higher core heat flux (Nolet et al., 2006) than commonly accepted (Lay et al., 2008).

A ponding plume in the mid-mantle, however, could still contribute to excess surface topography at hotspot swells. Surface topography reflects vertical normal stresses associated with flow generated by density anomalies within the mantle (e.g., Parsons and Daly, 1983). Ponding materials are thermally buoyant, resulting in positive vertical normal stress. In this study, we use topography kernels to quantify the relative magnitude of these stresses from density anomalies at depth. This method provides a quantitative way to test long-wavelength lower mantle structures against surface topography. The notion of topography kernel is valid when viscosity changes only in the vertical direction, but the ponding plume model provides a fortuitous situation that, due to its laterally expansive feature, allow such a simplified treatment of mantle viscosity. In the following analysis, we demonstrate that a thermal ponding plume has a significant influence on surface topography under most geometric and viscosity conditions.

2. Theoretical formulation

2.1 Buoyancy Flux and Plume Ponding

Plume buoyancy flux is defined as:

$$M = \int_0^R \Delta\rho(r)\, v(r)\, 2\pi r dr, (1)$$

where R is the radius of the model region, $\Delta\rho(r)$ is the density contrast between the plume material and ambient mantle, and $v(r)$ is the upwelling velocity (e.g., Olson et al., 1993). We assume $\Delta\rho(r)$ is constant across the crossection of plume upwelling and set it to $\alpha\rho_0 \Delta T$ where α is the thermal expansivity, ρ_0 is the reference density, ΔT is the average plume thermal anomaly relative to the ambient mantle. Under classical Poiseuille flow, $v(r) = 0$ when $R > a$ (plume radius) and $v(r)$ is expressed as:

$$v(r) = \frac{\alpha\rho_0\Delta T g}{4\mu_p}(a^2 - r^2)\ , \qquad (2)$$

where g is gravitational acceleration, and μ_p is the plume viscosity. Steady-state plume buoyancy flux may then be expressed as:

$$M = \frac{\pi(\alpha\rho_0\Delta T)^2 g a^4}{8\mu_p}, \qquad (3)$$

The relationship among plume viscosity, buoyancy flux, and radius is shown in Figure 2a. For a 400-km-radius plume of typical mantle viscosity, for example, predicted buoyancy flux is far greater than the existing estimates for the Hawaiian plume, which has the highest buoyancy flux among all plumes (e.g., Sleep, 1990). Typical buoyancy fluxes are on the order of 1000 kg/s. If such a large plume radius is applicable throughout the mantle, plume viscosity is required to be very high (Korenaga, 2005), or positive thermal buoyancy has to be substantially offset by negative chemical buoyancy (e.g., Lin and van Keken, 2006). Both possibilities represent considerable deviation from the conventional view of mantle plumes (e.g., Morgan, 1971; Richards et al., 1989).

The ponding plume model posits that a conduit radius can become smaller in the upper mantle, by deflecting some portion of the upwelling material in the mid-mantle. In this case, the geometry of material ponding at depth is constrained by the difference in the buoyancy fluxes of the upper and lower mantle plumes. Assuming, for simplicity, that the geometry of ponding materials is rectangular, we have:

$$M_L - M_U = (\alpha\rho_0\Delta T) v_p W H, \qquad (4)$$

where M_L is the buoyancy flux in the lower mantle, M_U is that in the upper mantle, v_p is plate velocity, W is the width of the ponding material, and H is its thickness. The thickness of the ponding material is thus inversely proportional to the width (Figure 2b). We use v_p as the horizontal velocity in the upper- and mid-mantle for simplicity; if the mid-mantle horizontal velocity is lower than the surface plate velocity, which is probably more realistic, it would lead to more pronounced ponding (i.e., greater H for a given W). When a plume in the lower mantle has a large radius and a low viscosity, the difference in buoyancy flux becomes unrealistically large, and even with an extreme width of 90° (10,000 km), the thickness of the ponding material exceeds the whole mantle depth. For the ponding plume model to be physically reasonable, therefore, plume radius in the lower mantle cannot be too large (<300 km), or the plume viscosity has to be relatively high ($\geq 10^{20}$ Pa s).

2.2 Topography Calculation

The topography kernel represents the sensitivity of surface topography to subsurface density perturbations. When the kernel takes a value of unity at some depth, for example, a density anomaly at that depth contributes fully to surface topography. Conventional isostasy calculation with a compensation depth is equivalent to assuming that the topography kernel is unity down to the compensation depth and becomes zero below. Whereas this assumption is reasonable when dealing with crustal-scale density anomalies, a more careful approach, such as using a topography kernel, is required to evaluate the influence of deep mantle structures on surface observables. The topography kernel can be constructed by calculating how vertical normal stress at the surface changes with the varying depth of a unit density anomaly (Parsons and Daly, 1983). In this study, we use the propagator matrix method to solve for the Stokes flow and derive such vertical normal stress (Hager and O'Connell, 1981). The notion of topography kernel is valid only when the spatial variation of viscosity is limited to the vertical direction. In the presence of lateral viscosity variations, surface topography based on the topography kernel is only an approximation, but it is sufficient for the discussion of long-wavelength topography (Richards et al., 1988), which is the focus of our analysis.

Once a topography kernel is generated, different distributions of density anomalies can be examined for their impact on surface topography. A negative density anomaly causes positive vertical normal stress, and in case of a ponding plume, ponding material beneath the MTZ is more buoyant than the ambient mantle, causing surface uplift. The topography kernel is a function of horizontal wavelength, and using equation (4), we set half of the wavelength to the width (W) of the ponding material as:

$$\frac{\lambda}{2} = W = \frac{\Delta M_p}{(\alpha \rho_0 \Delta T) v_p H}. \quad (5)$$

where λ is the wavelength and ΔM_p is the difference between M_L and M_U. Excess topography due to the ponding material, Δh_{excess}, can be calculated as:

$$\Delta h_{\text{excess}} = \frac{(\alpha \rho_0 \Delta T)}{\rho_0 - \rho_w} \int_{z_{\text{PMB}}}^{z_{\text{MTZ}}} T(z, \lambda)\, dz, \quad (6)$$

where z_{MTZ} and z_{PMB} (=z_{MTZ}+H) are the depth of the MTZ and lower extent of the ponding material, respectively, ρ_w is sea water density, and $T(z, \lambda)$ is the topography kernel.

3. Results

3.1 Topography Kernels

Topography kernels were calculated with horizontal wavelengths varying from 1450 to 20,000 km (Figure 3). In our formulation, the wavelength is twice the width of the ponding material. We used a simple 3-layer viscosity structure (e.g., Wei and Zhong, 2021) as well as one similar to that proposed by Mitrovica and Forte (2004), hereinafter referred to as MF04. The 3-layer viscosity structure features a 100-km stiff lid, low-viscosity upper mantle, and a high-viscosity lower mantle

(Figure 3c). Resulting topography kernels exhibit greater sensitivity in the upper mantle than in the lower mantle, particularly at shorter wavelengths. At longer wavelengths, kernels decrease more linearly from the top to the bottom. The MF04 viscosity structure is more complicated but results in similar topography kernels. Lower-mantle sensitivities, where plume material ponds, are higher in the MF04 kernels for shorter wavelengths. At longer wavelengths, the two sets of kernels become nearly identical. The only notable differences in sensitivity occur in the upper mantle at the shortest wavelengths, which are not relevant to material ponding below the MTZ. We also test modified viscosity structures in which the ponding material reduces the viscosity to that of the ponding material between z_{MTZ} and z_{PMB} by a factor of $\Delta\mu_p$. This reduction in viscosity generally leads to an increase in topographic sensitivity to sub-MTZ structure. These topography kernels do not account for the effects of lateral changes in viscosity, but ponding material is generally horizontally extensive (Figure 2b), so our kernel-based approach is deemed sufficient to quantify the first-order effects of ponding plume on long-wavelength topography. The kernels shown in Figure 3 are most appropriate for a ponding of an isolated mantle plume in the center of the ocean (e.g., the Hawaiian Plume).

3.2 Surface Topographic Response

Figure 4 shows representative examples of the geometry of ponding plumes with physically permissible ponding depths. The width of these structures is typically so large that it is difficult to illustrate them to scale. Figure 5 shows the excess topography generated by a ponding plume under four sets of viscosity profiles, including the 3-layer and MF04 background models, and their modified versions with plume viscosity. Only the topographic response generated by the thermal buoyancy of ponding material is plotted; all other sources of topography at a hotspot swell, such as the spreading of a narrow upper-mantle plume beneath the lithosphere, are absent in our calculation. In each case, 100 unique kernels were generated for ponding material of widths between 725 and 10,000 km. We conducted calculations for plumes with viscosities of 10^{19} Pa s and 10^{20} Pa s, under both original and modified background viscosity conditions. In all cases, the plume conduit in the upper mantle is fixed at 100 km in radius, plume material is 200 K hotter than the ambient mantle, reference mantle density ρ_0 just below the MTZ is 4500 kg/m^3, thermal expansivity α is $2.5 \times 10^{-5}\ \mathrm{K}^{-1}$, and plate velocity v_p is 7 cm/yr. The plate velocity is appropriate for the Hawaiian plume; the global average plate velocity is ~5 cm/yr (Parsons, 1981). Calculated excess topography for ponding plumes is on the order of tens of meters to a few kilometers (Figure 5). Topography is shown as a function of the thickness H of ponding material. Each H value is paired with a corresponding value of W, as shown in Figure 2b, for a given plume radius in the lower mantle and plume viscosity.

The topographic response under the 3-layer and MF04 viscosity profiles is shown in Figure 5a, for a ponding plume with a viscosity of 10^{19} Pa s. In this case, the buoyancy flux of the 100-km-radius plume in the upper mantle is about 17,300 kg/s, about twice the highest estimate for the Hawaiian plume (Sleep, 1990). Thinner (low H) and wider (high W) ponding material generally results in a greater topographic response, attributed to increased sensitivity to density perturbations at longer wavelengths. Due to the imposed maximum width of 90°, a ponding plume with a lower-mantle radius of 300 km and 400 km requires a physically improbable depth for ponding material, i.e., exceeding the core-mantle boundary (CMB). In these cases, the buoyancy fluxes for the lower-mantle plumes are massive, about 1.4×10^6 kg/s and 4.4×10^6 kg/s, respectively. For this plume viscosity, therefore, the lower-mantle conduit radius must be smaller than 200 km, to keep the concept of a ponding plume physically realistic. Even with the radius of 200 km and a physically permissible thickness of ponding material (i.e., H less than ~2000 km), however, excess topography is still greater than ~1 km. This is problematic, because the observed swell topography around the Hawaiian hotpot is on average only about 500 m (with a horizontal extent of ~1000 km). Because our calculation does not include the contribution from the spreading of the upper-mantle plume beneath the lithosphere, the excess topography from ponding material must be considerably lower than the swell topography to be consistent with the observed seafloor topography. To facilitate discussion, we assume that excess topography less than 100-200 m would be acceptable. Such condition can be satisfied by the narrowest plume considered here (with a lower-mantle radius of 150 km); but even this case requires material to pond almost to the CMB, to become undetectable in surface topography. As expected from its deeper sensitivity (Figure 3b), the MF04 viscosity profile generally yields greater topographic response than the 3-layer viscosity profile, thereby making a ponding plume more visible in surface topography.

Increasing plume viscosity to 10^{20} Pa s reduces upper- and lower-mantle buoyancy fluxes by an order of magnitude, but still, excess topography often exceeds the reasonable 100-200 m limit (Figure 5b). Under these conditions, the 100-km-radius plume in the upper mantle has a buoyancy flux comparable to a midsized plume such as Cape Verde and Réunion (Sleep, 1990). For a 400-km-radius lower-mantle plume, minimum excess topography is of ~2.6 km, far greater than is acceptable. A 300-km-radius lower-mantle plume can only produce acceptable excess topography with material ponding at a depth greater than the lower mantle, making this scenario physically unlikely as well. The two narrowest plumes (150 km and 200 km radii in the lower mantle) can satisfy our requirement for reasonable excess topography with physically realistic ponding geometries. These can be achieved with both background viscosity profiles, but the 3-layer structure generally produces less pronounced topography. In particular, a 150-km-radius lower-mantle plume generates under 200 m of excess topography for any given ponding thickness, making this the most reasonable scenario.

Unsurprisingly, a background viscosity profile modified by ponding material increases the magnitude of the surface uplift generated by a ponding plume. We set ambient lower-mantle viscosity to 10^{21} Pa s. Ponding material from a plume with a viscosity of 10^{19} Pa s thus reduces the background viscosity by two orders of magnitude (Figure 5c). Under these conditions, every examined ponding plume generates far more excess topography than is acceptable. The minimum surface expression of ponding material is ~800 m for the narrowest plume, attributed to a significant increase in topographic sensitivity generated by the viscosity reduction. Increasing the viscosity of the plume to 10^{20} Pa s, i.e., viscosity reduction only by one order of magnitude, generates similar excess topography as in the unmodified background viscosity profile (Figure 5d). The smaller viscosity reduction lessens its impact on kernel sensitivity. Only the two narrowest plumes generate plausible surface responses, similar to those found in the original background viscosity profile. In addition to the viscosity structures already discussed, a profile with a high-viscosity MTZ, a feature that could enhance plume ponding, was tested as well (Supplementary Figure 1). We find this viscosity structure to increase the surface response to ponding material under both unmodified and modified viscosity conditions (Supplementary Figure 2).

Even when narrow, relatively high-viscosity (10^{20} Pa s) lower-mantle plumes exhibit excess topography less than 100-200 m, the area underlain by the ponding material is still quite large. In the most favorable case, a 150-km-radius plume in the lower mantle with a viscosity of 10^{20} Pa s, the thickness of ponding material ranges from ~20 km to ~200 km with corresponding widths of 10,000 km to 725 km (equation 5). Additionally, our formulation sets an upper-mantle plume radius at the high end of estimates for conventional thermal plumes, a favorable condition for the ponding plume model; a narrower upper-mantle plume can transport much less material, increasing the total mass ponding below the MTZ and resulting excess topography.

4. Discussion and Conclusions

The majority of ponding plume geometries examined generate greater than acceptable excess topography, require a physically improbable ponding depth, or do both. For example, a ponding plume with a lower-mantle radius of 200 km and a viscosity 10^{19} Pa s (solid orange line in Figure 5c) could have a thickness as low as ~550 km, but requires a width of ~10,000 km (Figure 4b). Excess topography generated by such a structure is around ~1.5 km, much larger than is acceptable. A higher plume viscosity (10^{20} Pa s) with a radius of 300 km, similar to those imaged by seismic tomography, can fit within the lower mantle, but the excess topography is similar to that of narrower, less viscous plumes (Figure 5d). The scale of ponding material is so large that it would likely be detected by seismic tomography (Rickers et al., 2012). Yet, in the case of the Hawaiian plume, seismic tomography has not imaged such structure (Montelli et al., 2006; Fukao and Obayashi, 2013; Moulik & Ekström, 2014; French and Romanowicz, 2015), providing a major setback for the ponding plume model. Smaller plumes imaged with material ponding at the base of the MTZ (Nolet et al., 2006; Hansen et al., 2014) all have far less ponding material than is predicted by our modeling. Additionally, many well-resolved lower-mantle plumes are located closer than the width of many of these ponding geometries. More than one lower-mantle plume could feed into the same ponding region, resulting in even more ponding material and extreme excess topography.

Alternatively, one large ponding plume may source multiple plumes in the upper mantle, similar to a certain version of "superplume" (Maruyama, 1994; Courtillot et al., 2003). Such a condition may be present in the South Pacific Superswell, where multiple hotspots are located above one large slow seismic anomaly in the lower mantle (e.g., French and Romanowicz, 2015). Key features of superswells include non-age-progressive volcanic islands and long-wavelength excess topography on the order of ~500 m (McNutt, 1998; Adam and Bonneville, 2005). If multiple upper-mantle plumes draw from one superplume, the amount of ponding material is reduced, making a ponding plume more reasonable, but the large lower-mantle plume flux is still problematic. For example, a lower-mantle plume of 400 km radius has a buoyancy flux of ~4.4×10^6 kg/s, but even ten 100-km-radius plumes in the upper mantle only have a total buoyancy flux of ~1.7×10^5 kg/s (equation 3). Except for in the case of a 150-km-radius lower-mantle plume, which will not be able to form in this scenario because ten 100-km-radius plumes have a higher upper-mantle buoyancy flux than one 150-km-radius plume (equation 3), excess topography is too great (~1 km) for large-radius (>=300 km), low-viscosity plumes.

An alternative to multiple upper-mantle plumes is multiple plume heads. The head of a mantle plume can contain a significant volume of upwelling material. Bercovici & Mahoney (1994) proposed that the Ontong Java large igneous province (LIP) may be sourced from the same plume, if the plume head is able to separate from its conduit at the base of the MTZ. On the surface, a detached plume head is predicted to produce a "double LIP" where two different flood basalt provinces are observed, separated in time by ~ 30 Ma. Under this model, the older LIP forms from the initial plume head and the younger LIP forms when a secondary plume head, formed from the same conduit, reaches the surface. However, having two plume heads is not sufficient to account for the volume flux carried by a 100-km-radius upper-mantle plume with a viscosity of 10^{19} Pa s. In the case of Ontong Java, the maximum radius of a plume head is estimated to be 363 km

(Bercovici and Mahoney, 1994) and a total volume of ~2×10^8 km^3. It takes only ~15 Ma for a 100-km-radius plume to produce as much volume flux as two of such plume heads.

In this work, we seek to demonstrate the first-order impact of a ponding thermal plume. As such, second-order effects, such as the release of latent heat due to the endothermic phase change (e.g., Schubert et al., 1975), possible subadiabatic thermal gradients in the mid-mantle (e.g., Bunge, 2005), cycling of ponding material in large-scale mantle convection, are ignored. Thanks to the enormous surface manifestation of a typical ponding thermal plume, however, such details have a negligible impact on our assessment of this hypothesis. Many of our assumptions, such as large-radius (100 km) upper-mantle plumes and high plate velocity (7 cm/yr), are set in favor of the ponding plume model.

A few assumptions are potentially unfavorable to the ponding plume model, and we deem it necessary to address these in some detail. First, we assumed that ponding plumes are always in a steady state; however, owing to the large volume of ponding material, achieving a steady state takes a finite time. For the parameters examined, the time to fill the ponding geometries varies from ~5 Ma to ~11 Ma, depending on plume radius (Supplementary Figure 3). Since these times are shorter than the typical duration of hot spots (Ballmer et al., 2015) and high plate velocity is assumed, modeling a ponding plume in a steady state is justified. Second, we have assumed that the 670-km discontinuity was at a fixed depth. In the case of a hot anomaly, the 670-km discontinuity is expected to deflect upward (Bina and Helffrich, 1994), which should reduce the topographic response to material ponding below the MTZ. Assuming a Clayepron slope of -1.3 MPa/K (Fei et al., 2004), a pressure gradient of 43 MPa/km (Dziewonski and Anderson, 1981), a plume with $\Delta T = 200$ K deflects the phase transition by ~6 km upwards, resulting in a negligible change of the topography kernel and surface expression (Supplementary Figure 4). Finally, for our

3-layer viscosity model, we have assumed a large increase in viscosity occurs at the base of the MTZ. If significant viscosity stratification occurs at depth other than the 670-km discontinuity, a thermal plume may pond at this alternative depth. Recently, it has been suggested that two orders of magnitude increase in viscosity may exist at 1000 km depth (Rudolph et al, 2015; Deng and Lee, 2017). Modifying the 3-layer case to have a viscosity increase and ponding at 1000 km depth does reduce the surface topography, but it is still unreasonably large for wide (>=300-km-radius) mantle plumes (Supplementary Figure 5).

Although the preceding calculations and discussion focused on a purely thermal plume, it is also important to consider the possibility of thermochemical plumes because significant major-element heterogeneities have been suggested for several plumes including Hawaii and Iceland (e.g., Hauri, 1996; Takahashi et al., 1998; Korenaga and Kelemen, 2000; Sobolev et al., 2007). Previously, a dense chemical component has been invoked to explain large-radius mantle plumes (Farnetani and Samuel, 2005; Lin and vlan Keken, 2006; Dannberg and Sobolev, 2015). In our formulation, it is straightforward to evaluate the impact of chemical heterogeneities on surface topography, by means of the effective thermal anomaly (ΔT_{eff}). The Hawaiian plume, for example, has been suggested to contain ~20% recycled crustal material and have an excess temperature of ~200 K (Sobolev et al., 2007). Crustal material is ~100 kg/m^3 denser than the ambient mantle, so a plume with 20% recycled crust is intrinsically 20 kg/m^3 denser than the mantle, thereby offsetting the thermal buoyancy. Using $\alpha = 2.5 \times 10^{-5}$ K^{-1}, ρ_0 = 4500 kg/m^3, and $\Delta T = 200$ K, ΔT_{eff} is ~20 K. A factor of ten reduction in thermal anomaly lowers plume buoyancy flux by two orders of magnitude (equation 3), so even a thick (400-km-radius) thermochemical plume of typical viscosity (~6×10^{19} Pa s) can agree with the high end of buoyancy flux estimates for the Hawaiian plume (Figure 6). The lowest estimate for Hawaiian buoyancy flux can be achieved by a thick plume with a viscosity of ~2×10^{20} Pa s, lower than the viscosity of firm plumes ($10^{21} - 10^{23}$ Pa s; Korenaga, 2005). Conversely, with a recycled crust component, mantle plumes must have a radius greater than geodynamic predictions for thermal plumes (~100 km) to generate typical values of buoyancy flux (~1000 kg/s). This result agrees with previous buoyancy flux estimates for thermochemical plumes, but an eclogite content of 15 %, lower than estimates for Hawaii, has been shown to require an excess temperature of at least 550 K for a plume to reach the uppermost mantle (Dannberg and Sobolev, 2015). This is more than double the estimates for thermal anomalies constrained by plume chemistry (Soblev, et al., 2007), suggesting that recycled crust may not be able to reconcile thick plume conduits at depth with observed topographic swells.

We have shown, by simple numerical modeling, that ponding thermal plumes are an unlikely way to reconcile thick plume conduits in the lower mantle with observed topographic swells. Two of the remaining explanations are thermochemical plumes, as discussed above, and slowly upwelling plumes with grain-size-sensitive creep or viscoplastic rheology. As the latter possibility arises from lower-mantle rheology (Solomatov, 1996; Korenaga, 2005; Davaille et al., 2018), they can occur globally. On the other hand, it may seem ad hoc to invoke chemical heterogeneities for many thick plumes imaged by seismic tomography. Also, chemical heterogeneities in this context act to retard the upwelling of a plume and may require extreme excess temperatures, so it would be puzzling why the majority of plumes are dynamically compromised. However, if many plumes originate from large low-shear-velocity provinces (e.g., Burke and Torsvik, 2004), they may share similar chemical characteristics. Further improvement of seismic tomography, in conjunction with geochemical observations, will allow us to distinguish between these possibilities.

Acknowledgements: We would like to thank Editor Hans Thybo for his assistance with this manuscript. We thank Norm Sleep and two anonymous reviewers for their comments on the earlier version of the manuscript. This work was supported in part by U.S. National Science Foundation EAR-1753916.

References:

Adam, C., Bonneville, A., 2005. Extent of the South Pacific Superswell. J. Geophys. Res. Solid Earth. 110, B09408.

Ballmer, M.D., van Keken, P.E., Ito, G., 2015. Hotspots, large igneous province, and melting anomalies. Treatise on Geophysics. 7, 394-443.

Bercovici, D., Mahoney, J., 1994. Double flood basalts and plume head separation at the 660-kilometer discontinuity. Science. 266, 1367-1369.

Bina, C.R., Helffrich, G., 1994. Phase transition Clapeyron slopes and transition zone seismic discontinuity topography. J. Geophys. Res. Solid Earth. 99, 15,853–15,860.

Bunge, H.-P., 2005. Low plume excess temperature and high core heat flux inferred from non-adiabatic geotherms in internally heated mantle circulation models. Phys. Earth Planet. Inter. 153, 3-10.

Burke, K., Torsvik, T.H., 2004. Derivation of large igneous provinces of the past 200 million years from long-term heterogeneities in the deep mantle. Earth Planet. Sci. Lett. 227, 531-538.

Courtillot, V., Davaille, A., Besse, J., Stock, J., 2003. Three distinct types of hotspots in the Earth's mantle. Earth Planet. Sci. Lett. 205, 295-308.

Dannberg, J., Sobolev, S.V., 2015. Low-buoyancy thermochemical plumes resolve controversy of classical mantle plume concept. Nat. Comm. 6, 6960.

Davaille, A., Carrez, Ph., Cordier, P., 2018. Fat plumes may reflect the complex rheology of the lower mantle. Geophys. Res. Lett. 45, 1349-1354.

Davies, G.F., 1988. Ocean bathymetry and mantle convection: 1. Large-scale flow and hotspots. J. Geophys. Res. Solid Earth. 93, 10,467-10,480.

Deng, J., Lee, K.K.M., 2017. Viscosity jump in the lower mantle inferred from melting curves of ferropericlase. Nat. Comm. 8, 1997.

Dziewonski, A.M., Anderson, D.L., 1981. Preliminary reference Earth model. Phys. Earth Planet. Inter. 25, 297–356.

Farnetani, C.G., Samuel, H., 2005. Beyond the thermal plume paradigm. Geophys. Res. Lett. 32, 303–341.

Fei, Y., Orman, J.V., Li, J., Westrennen, W.V., Sanloup, C., Minarik, W., Hirose, K., Komabayashi, T., Walter, M., and Funakoshi. K., 2004. Experimentally determined postspinel transformation boundary in Mg_2SiO_4 using MgO as an internal pressure standard and its geophysical implications. J. Geophys. Res. Solid Earth. 109, B02305.

French, S., Romanowicz, G., 2015. Broad plumes rooted at the base of the Earth's mantle beneath major hotspots. Nature. 525, 95-99.

Fukao, Y., and M. Obayashi., 2013. Subducted slabs stagnant above, penetrating through, and trapped below the 660 km discontinuity. J. Geophys. Res. Solid Earth. 118, 5920–5938.

Hager, B., O'Connell, R.K., 1981. A simple global model of plate dynamics and mantle convection. J. Geophys. Res. Solid Earth. 86, 4843-4867.

Hager, B. H., Clayton, R. W., Richard, M. A., Comer, R. P., Dziewonski, A. M., 1985. Lower mantle heterogeneity, dynamic topography and the geoid. Nature. 313, 541-585.

Hansen, S.E., Graw, J.H., Kenyon, L.M., Nyblade, A.A., Wiens, D.A., Aster, R.C., Huerta, A.D., Anandakrishnan, S., Wilson, T., 2014. Imaging the Antarctic mantle using adaptively parameterized P-wave tomography: Evidence for heterogenous structure beneath West Antarctica. Earth Planet. Sci. Lett. 408, 66-78.

Hauri, E. H., 1996. Major-element variability in the Hawaiian mantle plume. Nature. 382, 415-419.

Hoggard, M.J., Parnell-Turner, R., White, N., 2020. Hotspots and mantle plumes revisited: Towards reconciling the mantle heat transfer discrepancy. Earth Planet. Sci. Lett. 542, 116317.

King, S.D., Adam, C., 2014. Hotspot swells revisited. Phys. Earth Planet. Inter. 235, 66-83.

Korenaga, J., 2005. Firm mantle plumes and the nature of the core-mantle boundary region. Earth Planet. Sci. Lett. 232, 29-37.

Korenaga, J., and Kelemen, P.B., 2000. Major element heterogeneity in the mantle source of the North Atlantic igneous province. Earth Planet. Sci. Lett. 184, 251-268.

Labrosse, S., 2002. Hotspots, mantle plumes and core heat loss. Earth Planet. Sci. Lett. 199, 147-156.

Leng, W., Gurnis, M., 2012. Shape of thermal plumes in a compressible mantle with depth-dependent viscosity. Geophys. Res. Lett. 39, L05310.

Lin, S.-C., van Keken, P.E., 2006. Dynamics of thermochemical plumes: 2. Complexity of plume structures and its implications for mapping mantle plumes. Geochem., Geophys., Geosyst. 7, Q03003.

Liu, X., Zhong, S., 2016. Constraining mantle viscosity structure for a thermochemical mantle using the geoid observation. Geochem., Geophys., Geosyst. 17, 895-913.

Maruyama, S., 1994. Plume tectonics. J. Geol. Sur. Japan. 100, 24-49.

McNutt, M.K., 1998. Superswells. Rev. Geophys. 36, 211-244.

Mitrovica, J.X., Forte, A.M., 2004. A new interface of mantle viscosity based on joint inversion of convection and glacial isostatic adjustment data. Earth Planet. Sci. Lett. 225, 177-189.

Montelli, R., Nolet, G., Dahlen, F.A., Masters, G., 2006. A catalogue of deep mantle plumes: New results from finite-frequency tomography. Geochem., Geophys., Geosyst. 7, Q11007.

Morgan, W. J., 1971. Convection in the lower mantle. Nature. 230, 42-43.

Moulik, P., Ekström, G., 2014. An anisotropic shear velocity model of the Earth's mantle using normal modes, body waves, surface wave, and long-period waveforms. Geophys. J. Int. 199, 1713-1738.

Nolet, G., Karato, S.-I., Montelli, R., 2006. Plume fluxes from seismic tomography. Earth Planet. Sci. Lett. 238, 685-699.

Olson, P., Schubert, G., Anderson, C., 1993. Structure of axisymmetric mantle plumes. J. Geophys. Res. Solid Earth. 98, 6829-6844.

Parsons, B., 1981. The rate of plate creation and consumption. Geophys. J. Int. 67, 437-448.

Parsons, B., Daly, S., 1983. Relationship between surface topography, gravity anomalies, and temperature structure of convection. J. Geophys. Res. Solid Earth. 88, 1129-1144.

Rickers, F., Fichtner, A., Trampert, J., 2012. Imaging mantle plumes with instantaneous phase measurements of diffracted waves. Geophys. J. Int. 190, 650-664.

Richards, M.A., Duncan, R.A., Courtillot, V.E., 1989. Flood basalts and hot-spot tracks: plume heads and tails. Science. 246, 103-107.

Richards, M.A., Hager, B.H., Sleep, N.H., 1988. Dynamically supported geoid highs over hotspots: Observation and theory. J. Geophys. Res. Solid Earth. 93, 7690-7708.

Rudolph, M. L., Lekic, V., Lithgow-Bertelloni, C., 2015. Viscosity jump in Earth's mid-mantle. Science. 350, 1349-1352.

Schubert, G., Yuen, D.A., Turcotte, D.L., 1975. Role of phase transitions in a dynamic mantle. Geophys. J. Int. 42, 705–735.

Sleep, N.H., 1990. Hotspots and mantle plumes: Some phenomenology. J. Geophys. Res. Solid Earth. 95, 6715-6736.

Sobolev, A.V., Hofmann, A.W., Kuzmin, D.V., Yaxley, G.M., Arndt, N.T., Chung, S.L., Danyushevsky, L.V., Elliott, T., Frey, F.A., Garcia, M.O., Gurenko, A.A., Kamenetsky, V.S., Kerr, A.C., Krivolutskaya, N.A., Matvienkov, V.V., Nikogosian, I.K., Rocholl, A., Sigurdsson, I.A., Sushchevskaya, N.M., Teklay, M, 2007. The amount of recycled crust in sources of mantle-derived melts. Science. 316, 412-417.

Solomatov, V. S., 1996. Can hotter mantle have a larger viscosity? Geophys. Res. Lett. 23, 937-940.

Takahashi, E., Nakajima, K., Wright, T.L., 1998. Origin of the Columbia River basalts: melting model of a heterogeneous plume head. Earth Planet. Sci. Lett. 162, 63-80.

Wei, M., Zhong, S., 2021. Constraints on mantle viscosity from intermediate wavelength geoid anomalies in mantle convection models with plate motion history. J. Geophys. Res. Solid Earth. 129, e2020JB021561.

Zhong, S., 2006. Constraints on thermochemical convection of the mantle from plume heat flux, plume excess temperature, and upper mantle temperature. J. Geophys. Res. Solid Earth. 111, B04409.

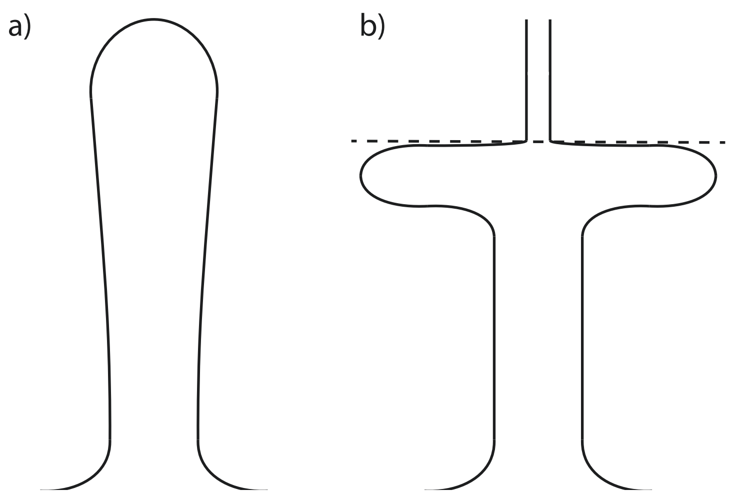

Figure 1. Two end-member geometries of plume conduits. (a) A firm (highly viscous) plume with a relatively slow accent velocity, and (b) a plume with low viscosity and material ponding beneath the 670 km discontinuity (dashed line).

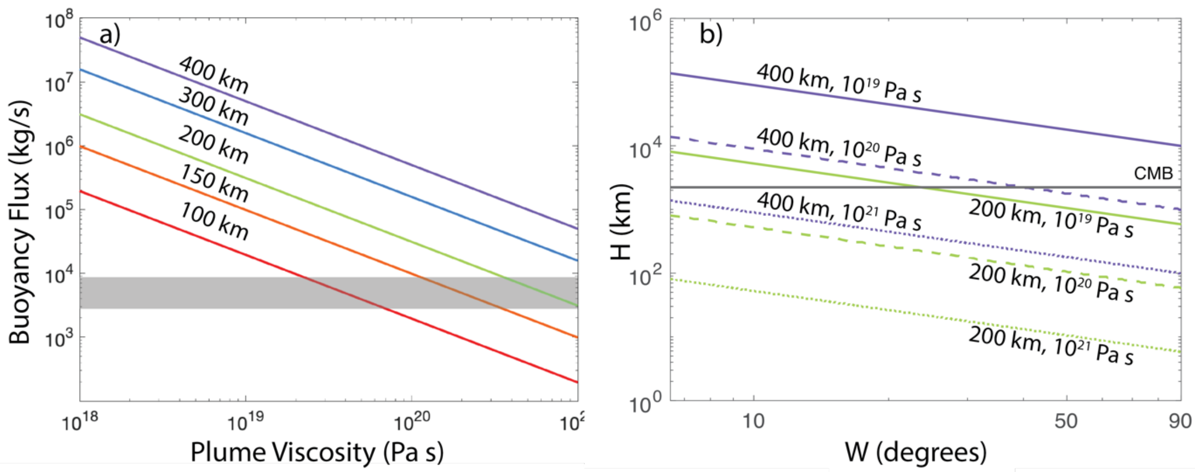

Figure 2. (a) Relationship between plume viscosity, buoyancy flux, and radius. Values above the curves represent the plume radius. Gray bar represents the low (Hoggard et al., 2020) and high (Sleep, 1990) buoyancy flux estimates for the Hawaiian plume. (b) Relationship between the thickness (H) and width (W) of ponding material (equation 4) for 200 km and 400 km lower plume radii and viscosities. The upper plume radius is fixed at 100 km, and plate velocity is assumed to be 7 cm/yr. Different line colors correspond to plume radii considered in (a), and solid, dashed, and dotted lines correspond to plume viscosity of 10^{19}, 10^{20}, and 10^{21} Pa s, respectively. Gray horizontal line denotes the depth of the core-mantle boundary; the values of H exceeding this line should be regarded as unrealistic.

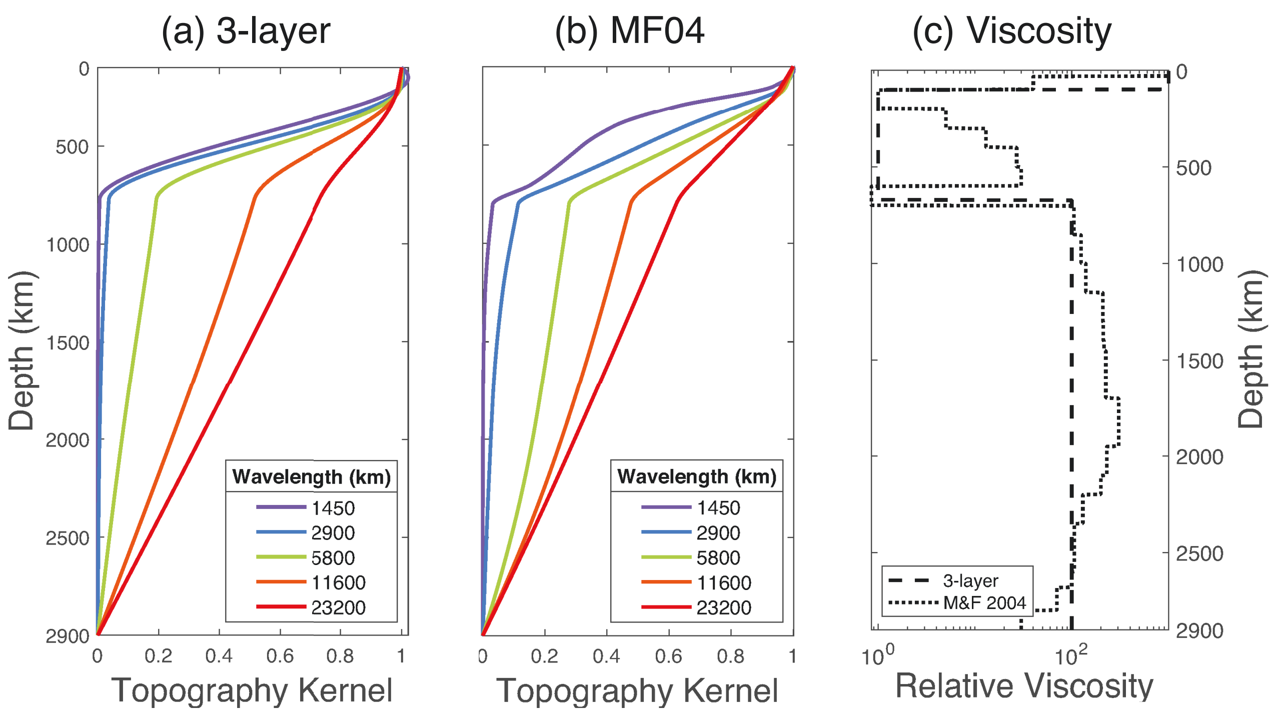

Figure 3. Topography kernels (a&b) calculated for various viscosity profiles (c). (a) is the 3-layer case, and (b) represents the profile of Mitrovica and Forte (2004).

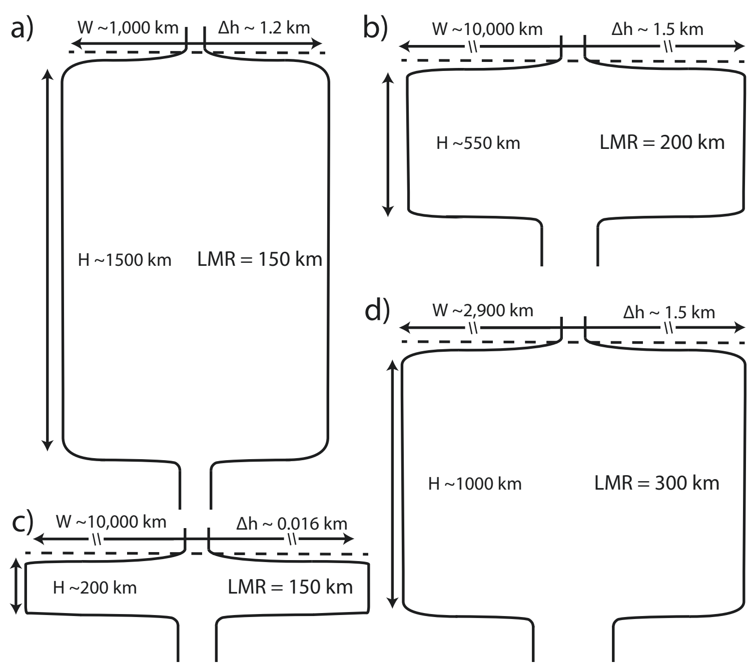

Figure 4. Schematic of representative ponding geometries modeled in Figure 5. W is ponding width, Δh is excess topography, H is ponding thickness, LMR is the lower mantle conduit radius. Upper and lower mantle plume radius, ponding thickness, and ponding width are to scale except for those with a break in arrows. (a,b) have μ_p of 10^{19} Pa s. (c,d) have μ_p of 10^{20} Pa s.

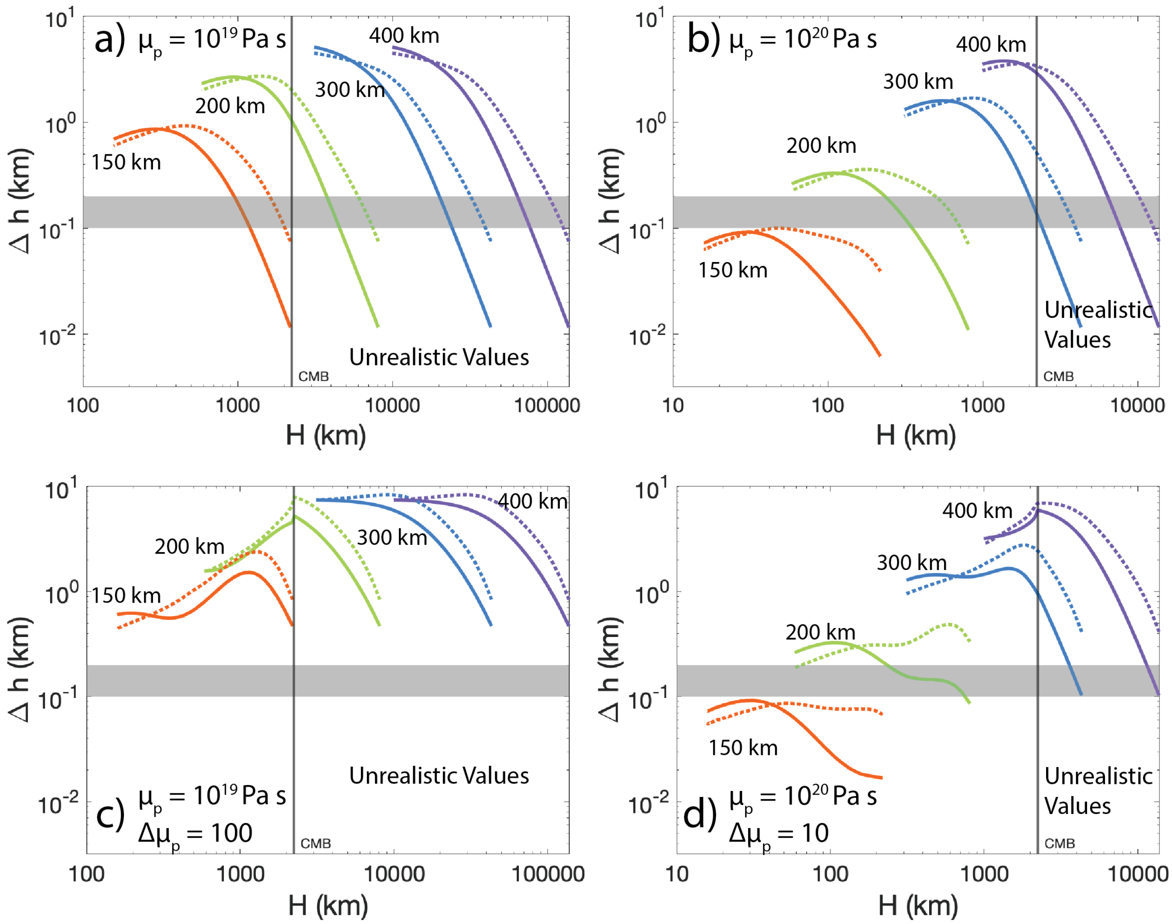

Figure 5. Surface topographic uplift due to a ponding plume at the bottom of the MTZ under various viscosity conditions. An unmodified viscosity structure is used in (a) and (b). (c) and (d) use a modified viscosity structure. μ_p is plume viscosity and $\Delta\mu_p$ is the factor by which ambient viscosity was reduced. The solid lines are the topographic response to the 3-layer derived kernels and the dotted lines are for MF04 derived kernels. Line color follows the same convention as Figure 2. The gray bar represents 100 m to 200 m of excess topography. The solid black line indicates the depth of the CMB, values beyond this are unrealistic.

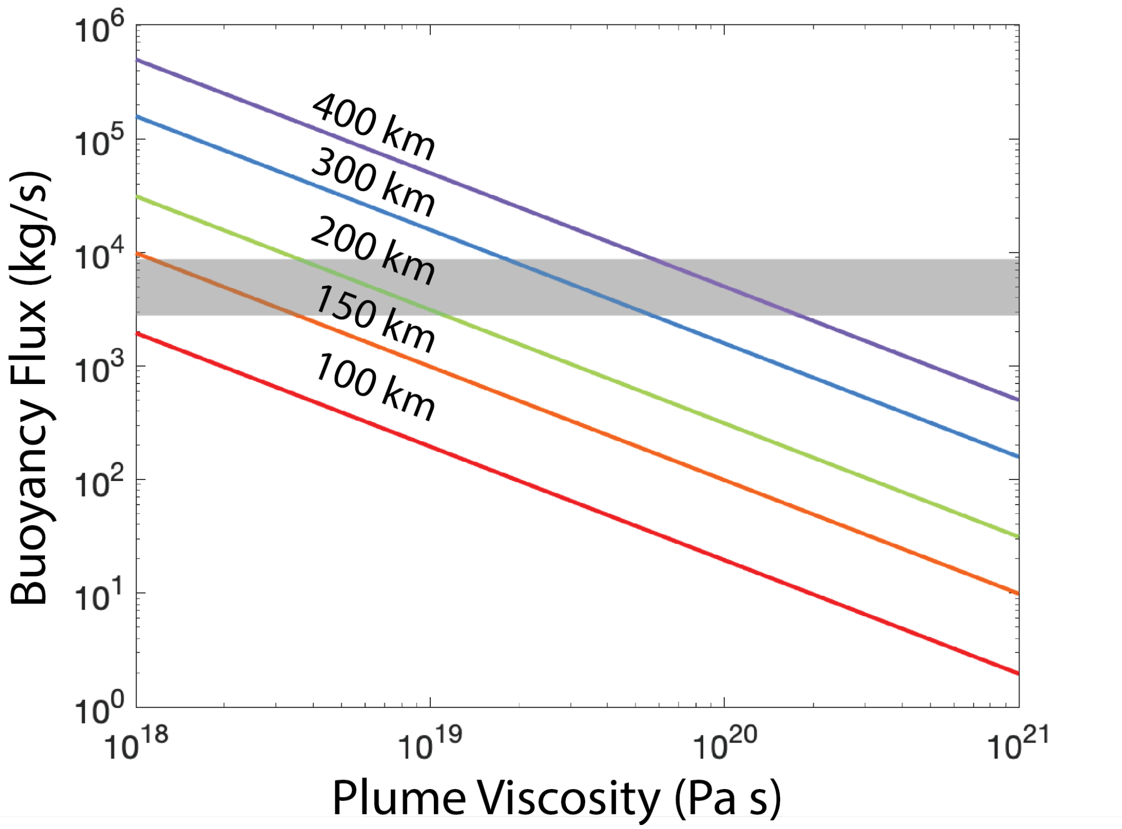

Figure 6. Relationship between plume viscosity, buoyancy flux, and radius for a thermochemical plume with the effective thermal anomaly (ΔT_{eff}) of 20 K. Values above the curves represent the plume radius. Gray bar represents the low (Hoggard et al., 2020) and high (Sleep, 1990) buoyancy flux estimates for the Hawaiian plume.

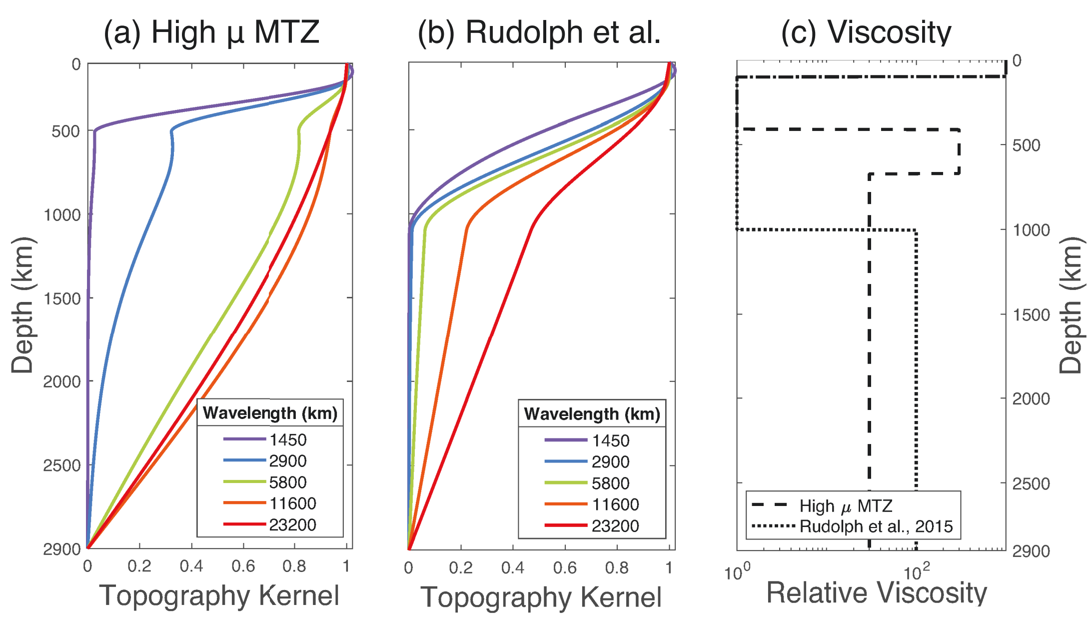

Supplementary Figure 1. Topography kernels (a&b) calculated for various viscosity profiles (c). (a) is a case with a high viscosity MTZ, and (b) represents a 3-layer case with the increase in viscosity occurring at the 1000 km depth as suggested by Rudolph et al., (2015).

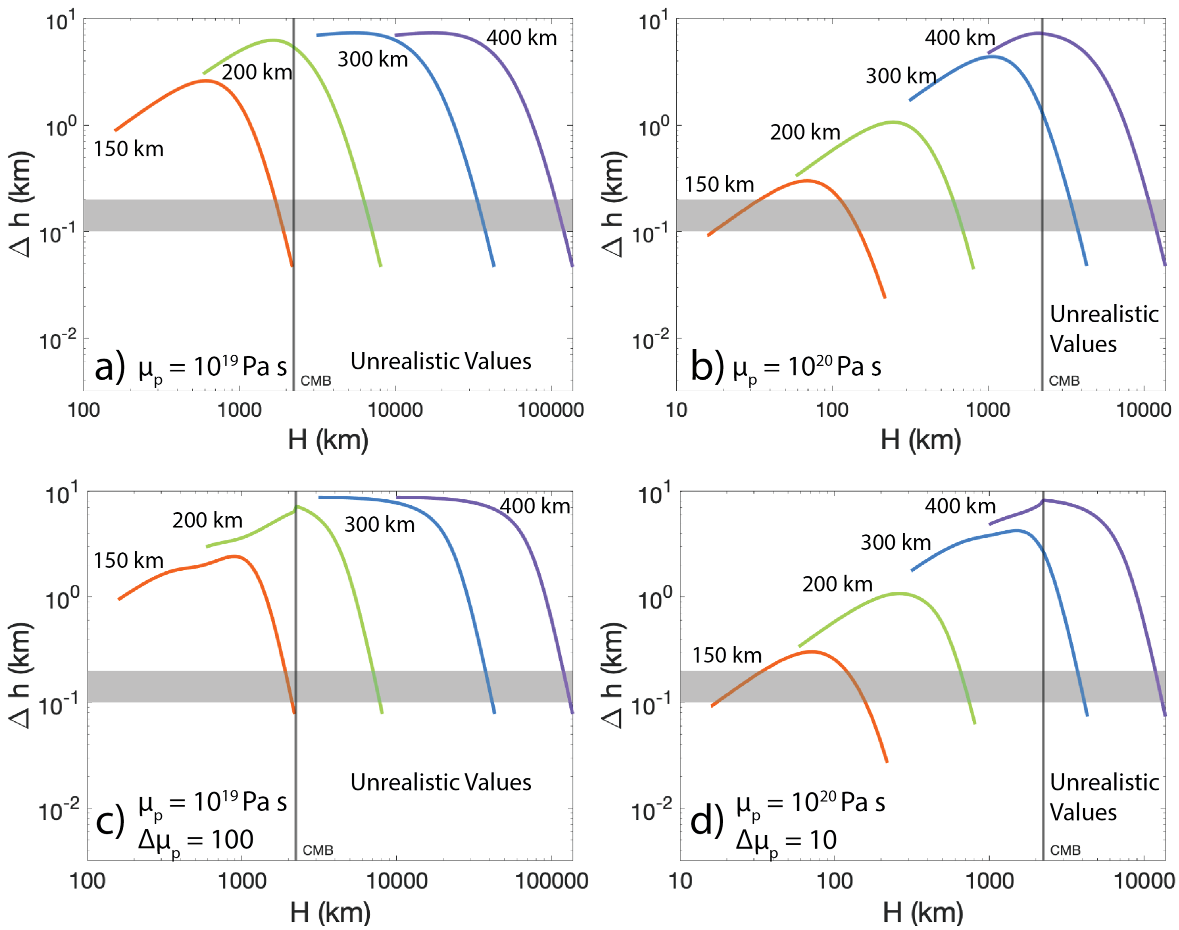

Supplementary Figure 2. Surface topographic uplift due to a ponding plume at the bottom of the MTZ under high viscosity MTZ derived kernels. An unmodified viscosity structure is used in (a) and (b). (c) and (d) use a modified viscosity structure. μ_p is plume viscosity and $\Delta\mu_p$ is the factor by which ambient viscosity was reduced. Line color follows the same convention as Figure 2. The gray bar represents 100 m to 200 m of excess topography. The solid black line indicates the depth of the CMB, values beyond this are unrealistic.

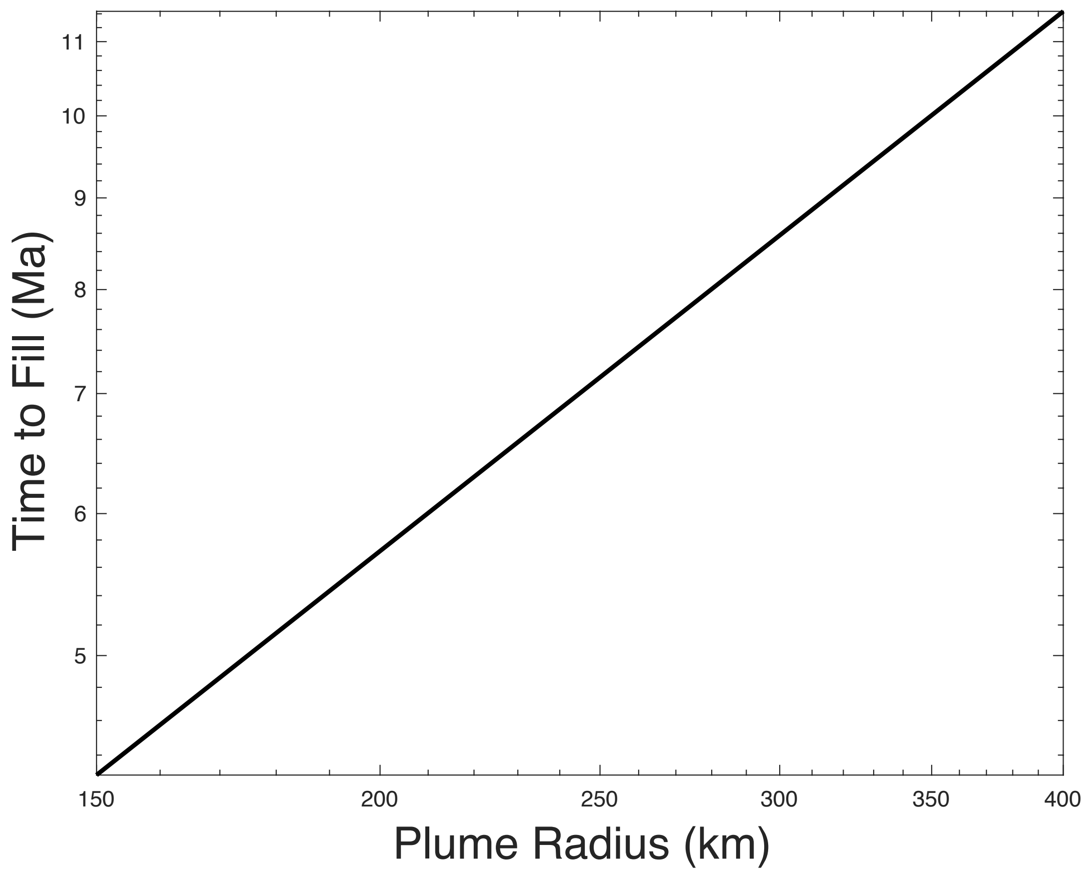

Supplementary Figure 3. Time to fill the examined ponding geometry compared to lower-mantle plume radius. This is only a function of plume radius and plate velocity ($t = a/v_p$). The plate velocity is fixed at 7 cm/yr.

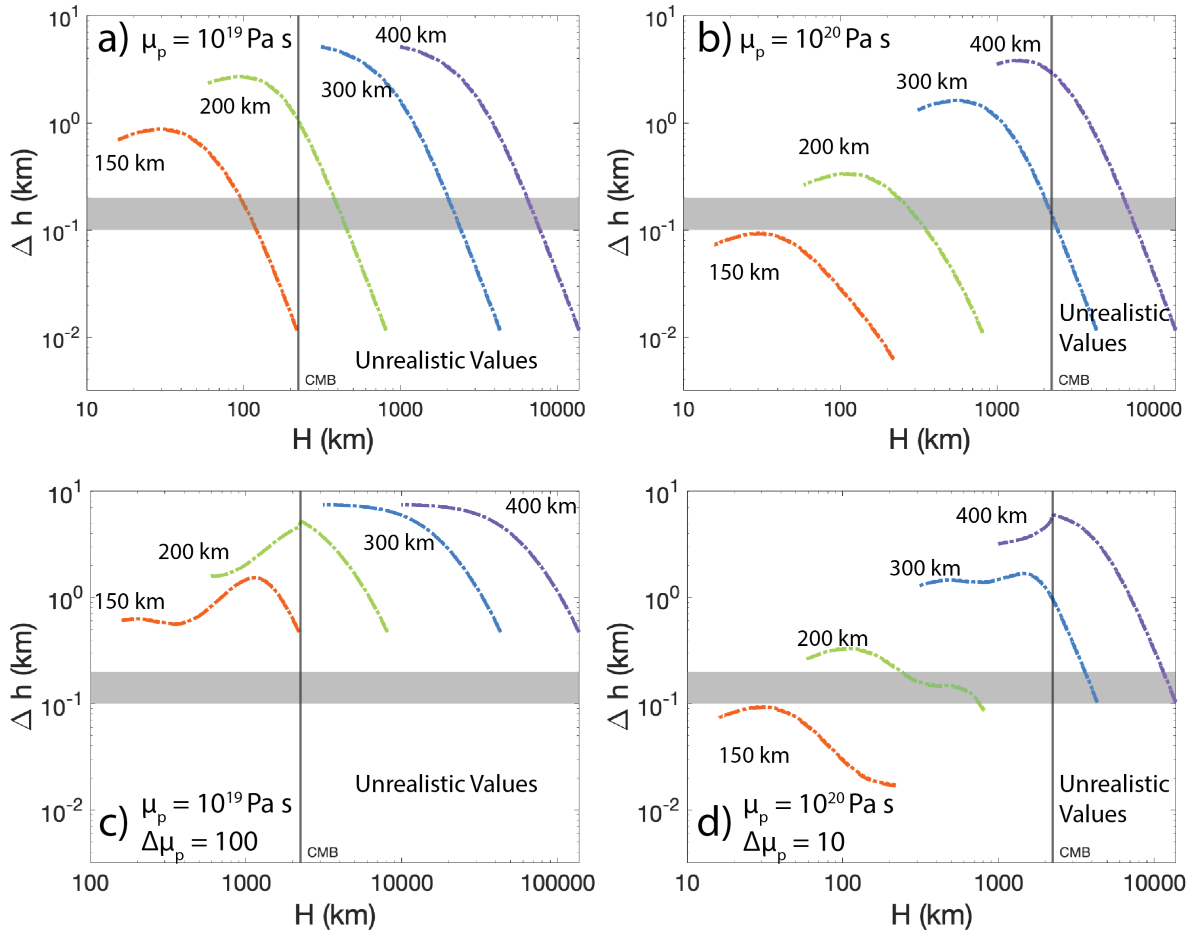

Supplementary Figure 4. Surface topographic uplift due to a ponding plume at the bottom of the MTZ under 3-layer viscosity structures. The dashed lines are the topographic response to a fixed 670-km discontinuity and the dotted lines are for kernels derived from a 670-km discontinuity displaced upwards by ~6 km. An unmodified viscosity structure is used in (a) and (b). (c) and (d) use a modified viscosity structure. μ_p is plume viscosity and $\Delta\mu_p$ is the factor by which ambient viscosity was reduced. Line color follows the same convention as Figure 2. The gray bar represents 100 m to 200 m of excess topography. The solid black line indicates the depth of the CMB (set to 670 km); values beyond this are unrealistic.

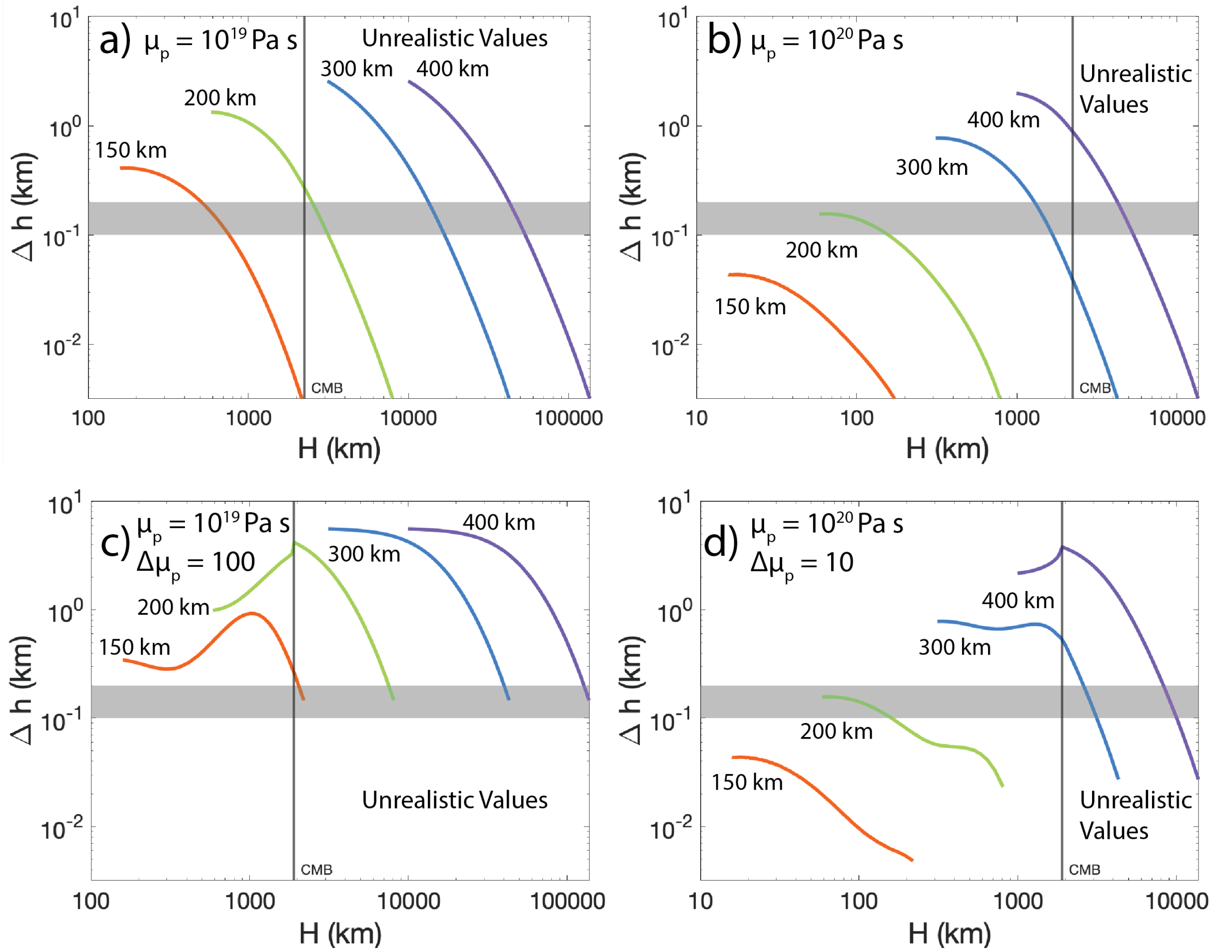

Supplementary Figure 5. Surface topographic uplift due to a ponding plume at 1000 km depth with a 3-layer viscosity model with the two orders of magnitude increase at 1000 km depth as in Rudolph et al. (2015). See Supplementary Figure 1b for the kernels used. An unmodified viscosity structure is used in (a) and (b). (c) and (d) use a modified viscosity structure. μ_p is plume viscosity and $\Delta\mu_p$ is the factor by which ambient viscosity was reduced. The gray bar represents 100 m to 200 m of excess topography. The solid black line indicates the depth of the CMB; values beyond this are unrealistic.